INL/JOU-23-70846-Revision-0

Thermal conductivity suppression in uranium-doped thorium dioxide due to phonon-spin interactions

May 2024

Zilong Hua, Saqeeb Adnan, Amey Rajendra Khanolkar, Karl Rickert, David Turner, Timothy Prusnick, James Matthew Mann, David H Hurley, Marat Khafizov, Cody Dennett

Changing the World's Energy Future

Idaho National Laboratory

INL is a U.S. Department of Energy National Laboratory operated by Battelle Energy Alliance, LLC

INL/JOU-23-70846-Revision-0

Thermal conductivity suppression in uranium-doped thorium dioxide due to phonon-spin interactions

Zilong Hua, Saqeeb Adnan, Amey Rajendra Khanolkar, Karl Rickert, David Turner, Timothy Prusnick, James Matthew Mann, David H Hurley, Marat Khafizov, Cody Dennett

May 2024

Idaho National Laboratory
Idaho Falls, Idaho 83415

http://www.inl.gov

Prepared for the
U.S. Department of Energy
Under DOE Idaho Operations Office
Contract DE-AC07-05ID14517

Journal of Materiomics 10 (2024) 709–715

Contents lists available at ScienceDirect

Journal of Materiomics

journal homepage: www.journals.elsevier.com/journal-of-materiomics/

Research paper

Thermal conductivity suppression in uranium-doped thorium dioxide due to phonon-spin interactions

Zilong Hua [a, *], Saqeeb Adnan [b], Amey R. Khanolkar [a], Karl Rickert [c], David B. Turner [d], Timothy A. Prusnick [c], J. Matthew Mann [e], David H. Hurley [a], Marat Khafizov [b, **], Cody A. Dennett [a, f]

[a] Materials Science and Engineering Department, Idaho National Laboratory, Idaho Falls, ID, 83415, USA
[b] Department of Mechanical and Aerospace Engineering, The Ohio State University, Columbus, OH, 43210, USA
[c] KBR, Dayton, OH, 45431, USA
[d] Azimuth Corporation, Fairborn, OH, 45324, USA
[e] Air Force Research Laboratory, Wright-Patterson AFB, OH, 45433, USA
[f] Department of Nuclear Science and Engineering, Massachusetts Institute of Technology, Cambridge, MA, 02139, USA

ARTICLE INFO

Article history:
Received 20 September 2023
Received in revised form
6 November 2023
Accepted 10 November 2023
Available online 5 December 2023

Keywords:
Phonon-spin interactions
Thermal conductivity
U—ThO_2 system

ABSTRACT

In this work, impact of low level of uranium (U) atom substitution on thermal conductivity of thorium dioxide (ThO_2) is investigated. ThO_2 is an electronic insulator with a wide optical band-gap and no unpaired electrons whose thermal transport is governed by phonons. U-substitution introduces unpaired *f*-electrons resulting in paramagnetic behavior of U–ThO_2 at room temperature, which significantly suppresses its thermal conductivity. A single crystal of U–ThO_2 with graded composition of U is grown using a hydrothermal synthesis method, and thermal conductivity measurements are performed in regions with uniform composition of U at levels of 0%, 6%, 9% and 16%. Measured thermal conductivity profiles over 77–300 K temperature range are analyzed using an analytical expression for phonon-mediated thermal transport based on Klemens-Callaway model. Temperature dependent thermal conductivity is found to deviate significantly from the Rayleigh scattering trend expected for a simple substitutional point defect with a small perturbation to mass and interatomic forces. With the resonant scattering term, observed large suppression of thermal conductivity at low temperatures can be closely reproduced. Additionally, the extracted phonon-spin coupling constants imply a nonlinear relation of phonon-spin interaction intensity with respect to U doping percentage. Our study reveals how phonon-spin scattering contributed by unpaired *f*-electrons in U atoms influences thermal transport in the U–ThO_2 system.

1. Introduction

Dopants play a key role in thermal transport in fluorite oxides across a range of energy applications including solid oxide fuel cells [1], thermal barrier coatings [2], laser host materials, thermoelectrics [3], and nuclear fuels [4]. In oxide materials, thermal energy is primarily conducted by lattice vibrations, namely, phonons [5]. Dopants acting as point defects (substitutional impurities or interstitials) scatter phonons, suppressing thermal conductivity [6]. Traditionally, such point-defect-induced thermal conductivity suppression in the actinide fluorite oxides has been described using a Rayleigh scattering formulation [7–10]. However, for certain point defects, Rayleigh's formulation fails to explain low-temperature thermal transport behavior due to phonon interactions with localized vibrational modes [11–17]. In the case of paramagnetic impurities, the interaction between the point defect impurities and the surrounding host lattice, through modulation of the crystalline electric field, induces a spin transition by perturbing the orbital motion of paramagnetic electrons. The spin transition energy is imparted to the host lattice leading to a localized (resonant) mode that gives rise to phonon-spin interactions, or phonon resonant scattering [18–20]. Phonon-spin interactions have a

* Corresponding author.
** Corresponding author.
E-mail addresses: zilong.hua@inl.gov (Z. Hua), khafizov.1@osu.edu (M. Khafizov).
Peer review under responsibility of The Chinese Ceramic Society.

https://doi.org/10.1016/j.jmat.2023.11.007

characteristic effect on low temperature thermal conductivity, tending to introduce a dip in thermal conductivity where one typically expects maximum thermal conductivity with Rayleigh-type scattering only. In some cases, the thermal conductivity reduction induced by phonon-spin interactions can be orders of magnitude higher than that induced by Rayleigh-type scattering [21,22].

Thoria (ThO_2) has been considered a promising candidate material for advanced nuclear fuel cycles due to its high melting point, reasonable thermal conductivity, and relatively low radioactive waste footprint [23]. Recently, a number of works have focused on better understanding the thermal and mechanical properties of thoria and the possible changes of these properties induced by defects generated in extreme nuclear reactor environments. The use of high-quality single crystal thoria has been the critical foundation of these works, as desired microstructure features can thus be introduced in isolation [4]. Specifically, thermal conductivity, and corresponding changes induced by point defects and dislocation loops, have been investigated by Dennett, Deskins, Jin, and coworkers [24–28], by combining the efforts of advanced experimental tools (laser-based thermoreflectance and transmission electron microscopy) and state-of-the-art modeling approaches (linearized Boltzmann transport equation solutions with inputs from first principles calculations, defect evolution models, and advanced electron microscopy characterization, *etc.*).

In this work, we further explore how phonon-spin interactions impact the thermal conductivity of thoria by doping single crystal thoria with uranium (U). Tied to the magnetic properties owing to unpaired U-ion, phonon-spin interactions have been reported responsible for the remarkably lower thermal conductivity of UO_2 comparing to the isostructural ThO_2[29]. The phonon-spin interactions induced breakdown of cubic symmetry of UO_2 lattice, or Jahn-Teller distortion, was further applied to explain the observed thermal anisotropy in this cubic compound [30]. A more recent study reported that the Jahn-Teller distortion also exists in the U–ThO_2 system, and the distortion of the oxygen cage of UO_2 unit cell introduces the λ-type anomalies in heat capacity of the U–ThO_2 system at low temperature [31]. Here, local thermal conductivity (k) in a temperature range (T) of 77–300 K was measured on a U-doped thoria sample. By using a hydrothermal synthesis technique, varied U doping was introduced in isolated spatial regions from a single crystal thoria seed. Three iso-concentration regions with uniform U-doping percentages (6%, 9% and 16%) were identified using Raman spectroscopy and X-ray fluorescence (XRF), and then fiducially marked using a focused-ion-beam (FIB) for thermoreflectance measurements. The extracted k–T curve is compared with that calculated from a Klemens-Callaway thermal transport model to isolate the impacts of Rayleigh-type phonon-point defect scattering and phonon-spin interactions on thermal conductivity. We find that phonon-spin interactions contribute more than Rayleigh-type scattering to the thermal conductivity reduction in this temperature range, and the correlated intensity does not linearly increase with the doping level.

2. Experimental section

2.1. Crystal preparation

Crystal synthesis followed the previously published procedure for hydrothermal synthesis of $(U,Th)O_2$, with a feedstock composed of 0.2 g of UO_2 (IBI Labs, 99.99) and 2.1 g of ThO_2 (IBI Labs 99.99) [32]. The bottom 127 mm of the silver growth ampoule was heated to 650 °C over 4.5 h. The top 139.7 mm was heated to 525 °C over 4.5 h, paused at 525 °C for 18 h, and then heated to 600 °C over 2 h. These temperatures were held for 45 days at a pressure of 23.5 kpsi (1 kpsi = 6,895 kPa) before being cooled to 10 °C over 24 h. The product was bisected with a water-cooled diamond wire saw (STX-202P, MTI Corporation) to obtain halves with the largest surface area. The cut face was polished on a rotary disc polisher with diamond laps, ending with a 0.1 μm grit size.

2.2. Iso-concentration region analysis

μ-Raman spectroscopy and XRF were used to identify different iso-concentration regions for thermal transport analysis and to measure the as-grown uranium concentrations, respectively. The Raman and XRF maps, an optical image of the as-polished crystal, and XRF line scans of the iso-concentration region are shown in Fig. 1. A summary of the Raman and XRF analyses are provided here and further details can be found in the Supplementary Materials.

μ-Raman measurements were carried out using a Renishaw Invia Reflex Raman microscope with a 633 nm excitation source equipped with 1,200 l/mm dispersion grating and a standard Renishaw Si CCD [33]. A Si calibration was performed prior to the measurements. The laser was focused through a 50 × long-working-distance objective with a numerical aperture (NA) of 0.5. A μ-Raman map of the polished side of the growth region was performed with a single 0.5 s exposure for each point and points were collected in 2 μm by 2 μm intervals. The laser focus was manually adjusted every 50 μm and the intervening focal points were extrapolated. Renishaw Raman spectroscopy software WiRE was used to calculate and plot the signal to baseline intensity and full peak width at half of the maximum intensity (FWHM) for the T_{2g} peak.

XRF data were collected using two large-area silicon drift detectors set to a 40 keV range on a Bruker M4 TORNADO^{PLUS}, with an Rh source set at 50 kV and 300 μA, and a spot size of 14.7 μm (independently measured on this specific instrument). An XRF map of the polished side of the growth region was taken and spots were analyzed every 4 μm (in both x and y directions). The dwell time was 50 ms/pixel, with each pixel being 4 μm in diameter, and 15 cycles were performed and averaged together. A Zr calibration was performed prior to measurements being taken. Visual inspection of the overall XRF spectrum of each map was used to initially determine which elements may be present. In all cases, peaks that did not match U or Th did not reasonably match any other elements, thus only U and Th were included in the quantification step.

2.3. Thermal transport measurements

Local thermal transport was measured using a spatial domain-thermoreflectance (SDTR) technique [34,35]. In SDTR, a continuous-wave (CW) laser (Coherent OBIS 660 nm) with a periodically modulated intensity is used to locally heat the sample and induce a thermal wave. The propagation of the thermal wave is detected using a CW laser with constant intensity (Coherent Verdi 532 nm) through the thermoreflectance effect [34]. Thermal transport properties, such as thermal conductivity and thermal diffusivity, can be extracted using a thermal diffusion model and corresponding boundary conditions [34–36]. In order to improve the measurement spatial resolution, laser beams are focused using a 50 × long-working-distance objective lens (Olympus SLMPlan 50 ×). The spot size on the sample surface is ~1 μm for each laser, with the power of ~2 mW and ~0.3 mW for the heating and probe lasers, respectively.

Thermal transport property measurements were conducted in the iso-concentration regions and in the seed ThO_2 area over a 77–300 K temperature range with a step of 25 K and temperature fluctuation of less than 3 K[26]. At each temperature, at least 6 sets of measurements at four modulation frequencies, 10, 20, 50 kHz and

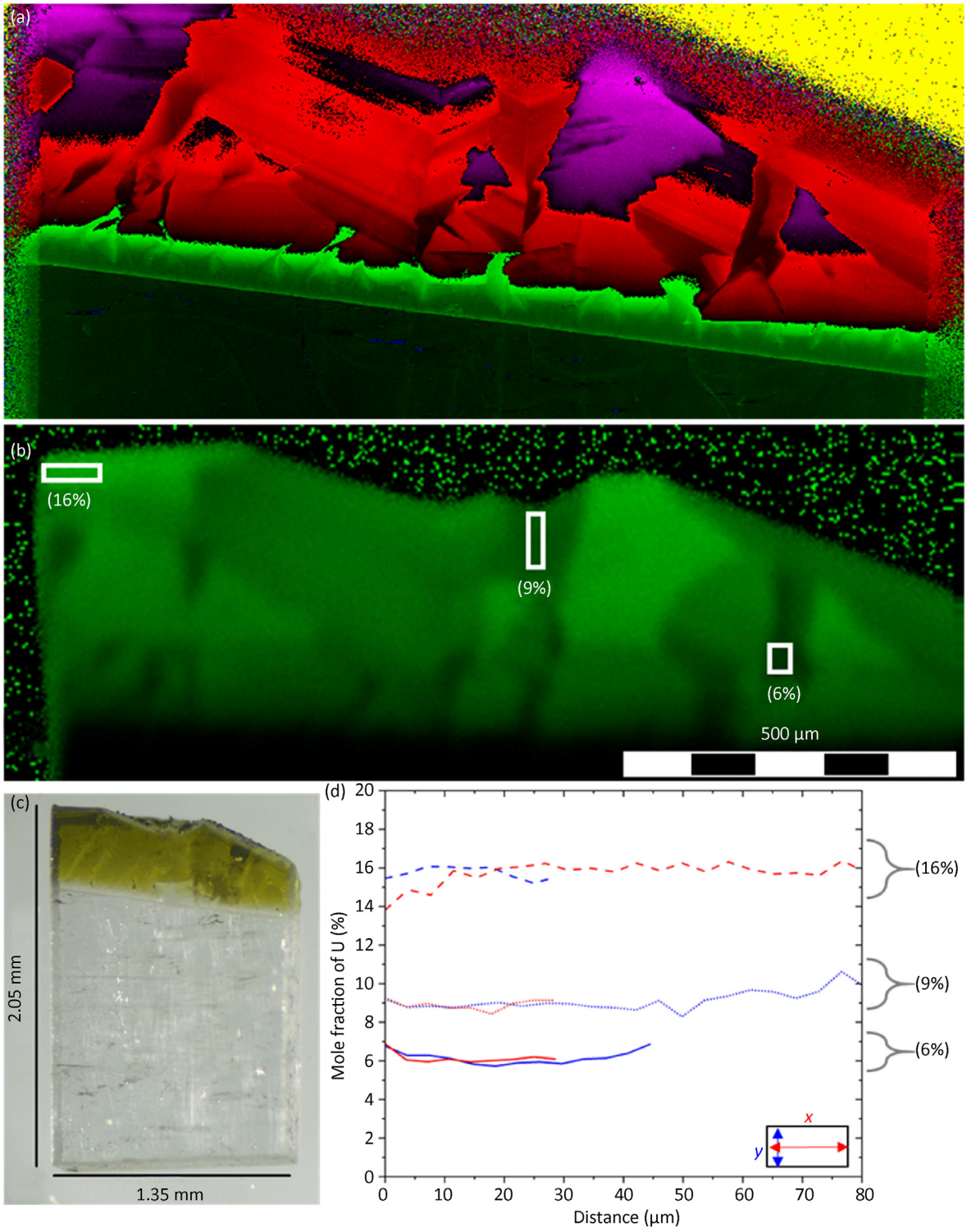

Fig. 1. (a) μ-Raman map showing spatial variation of T_{2g} FWHM of the $U_xTh_{1-x}O_2$ region and ThO_2 seed (purple = broad peak indicating more defects/doping, dark green = narrow pure thoria peak); (b) XRF map of the same showing U signal intensity; (c) Optical image of the entire as-prepared crystal; and (d) XRF line scans showing atomic composition across the iso-concentration regions drawn in (b).

100 kHz, were performed to statistically reduce the uncertainty of measured thermal conductivity. A 63 nm film of gold was sputter-coated on the sample surface to improve the thermoreflectance effect and energy absorption at this heating laser wavelength [37]. This film thickness was chosen based on a sensitivity analysis to ensure independent extraction of thermal conductivity (k) and thermal diffusivity (D) at room temperature. At room temperature, the SDTR thermal model can be validated by calculating the heat capacity (C_p) from measured k and D and comparing it to reference measurements made on crystals using the same growth process [24]. At low temperature, D was the sole parameter optimized from SDTR measurements to improve accuracy; k was then calculated at

each temperature as $k = D\rho C_p$, where C_p and density (ρ) for pure ThO_2 was obtained from previously reported values [24]. In U-doped regions, C_p of pure ThO_2 was used as the estimation of C_p values for U-doped ThO_2 as the heat capacity of pure fluorite UO_2 varies little from that of ThO_2 in this temperature range [4,31].

3. Results and discussion

The measured thermal diffusivity (D) and calculated thermal conductivity (k) in the 6%, 9% and 16% U doped ThO_2 regions, and in the seed ThO_2 region, of the heterogeneous

Crystal are plotted in Fig. 2. The standard errors determined on the basis of multiple measurements at each concentration and temperature are ~5% for the majority of concentrations and temperatures. In the seed ThO_2 at 125 K, the uncertainty is slightly higher (~10%) due to the high diffusivity at low temperatures and challenges associated with stabilizing this temperature using LN_2 coolant. In the seed ThO_2, k at 77 K is measured as 117 W/m·K, comparable to the highest reported value of k for single crystal ThO_2 at the same temperature [38] and matching the results from first principle calculation [26,28]. This suggests low impurity levels in the seed crystal. After doping, there are significant reductions in both k and D over the entire temperature range. The relative change in k increases as the temperature decreases. A slight hump is observable in the k–T curve between 125 and 175 K in all U-doped regions. This feature is not reflected in the ThO_2 seed, nor is it expected based on previous measurements of hydrothermally-grown ThO_2 single crystals [26,38,39]. In later sections, it will be shown that this hump is corresponding to the phonon-spin interaction introduced by U atoms. The thermal conductivity of 9% U doped ThO_2 does not differ noticeably from that at 6% U-doping: 12.6 W/(m·K) for the 9% doped region *versus* 12.9 W/(m·K) for the 6% doped region at 77 K. However, with additional doping to 16%, a significant thermal conductivity reduction was observed: 6.6 W/(m·K) at 77 K, or ~50% lower than the 9% doped region.

We analyze our results using a Klemens-Callaway model (KCM) to investigate the impact of individual phonon scattering mechanisms on thermal conductivity. As a simplified analytical model version of Boltzmann transport equation, KCM has been widely used to approximate phonon mediated thermal conductivity in past decades. Although it was reported that KCM can be inaccurate when handling complex momentum relaxation processes with different phonon frequency dependencies [40], it is still proven capable of providing reasonable approximations of lattice thermal conductivity in an efficient way [41]. Using Debye's linear approximation for phonon dispersion, thermal conductivity of our U doped ThO_2 system is calculated as:

$$k = \frac{1}{2\pi^2 v^3}\int_0^{\omega_D} \frac{C(\omega,T)v^2\omega^2}{\tau^{-1}(\omega,T)}\mathrm{d}\omega \tag{1}$$

where ω is phonon frequency, T is temperature, ω_D is the Debye frequency, and v is the sound velocity [42,43]. The Debye sound velocity is expressed through the longitudinal (v_L) and transverse (v_T) components as $v = \left({}^{1}\!/_{3v_L^3} + {}^{2}\!/_{3v_T^3}\right)^{-1/3}$. The sound velocity components v_L and v_T are obtained through elastic stiffness tensor elements C_{11} and C_{44}, as $v_L = \sqrt{C_{11}/\rho}$.

And $v_T = \sqrt{C_{44}/\rho}$. Values of the elastic stiffness tensor components for pure ThO_2 are used as reported in Refs. [44,45] and the Debye sound velocity was calculated to be 3,165 m/s. The Debye frequency is calculated as $\omega_D = v(6N\pi^2/V_0)^{1/3}$, where $N = 3$ is the number of atoms in the fluorite unit cell, and $V_0 = a^3/4$ is the volume of the unit cell, where $a = 5.529$ Å is the lattice constant of pure ThO_2[46]. The specific heat, $C(\omega,T)$ is expressed as:

$$C(\omega,T) = \frac{k_B x^2 e^x}{(1-e^x)^2} \tag{2}$$

where $x = h\omega/k_BT$, k_B is the Boltzmann constant, and h is the reduced Planck's constant. The scattering rate τ^{-1} is a combination of multiple scattering processes that are summed using Matthiessen's rule as:

$$\tau^{-1} = BT\exp\left(-\frac{T_D}{3T}\right)\omega^2 + A_i\omega^4 + \frac{V_0}{4\pi N v^3}\Gamma\omega^4 + \frac{C_r\omega^4}{\left(\omega^2-\omega_0^2\right)^2}F(\omega_0,T) \tag{3}$$

where each term in Eq. (3) represents an individual scattering process [6,43,47]. The first term corresponds to three-phonon scattering, where $T_D = \hbar\omega_D/k_B$ is the Debye temperature. The second term quantifies the contribution from impurities in the pristine sample, described here by Rayleigh-type scattering of phonons as has been successful in the past for ThO_2 [26,28]. These two scattering processes exist in both seed thoria and U-doped thoria, and the corresponding linear parameters can be obtained by fitting the measured k–T profile of seed thoria to the KCM using only the first

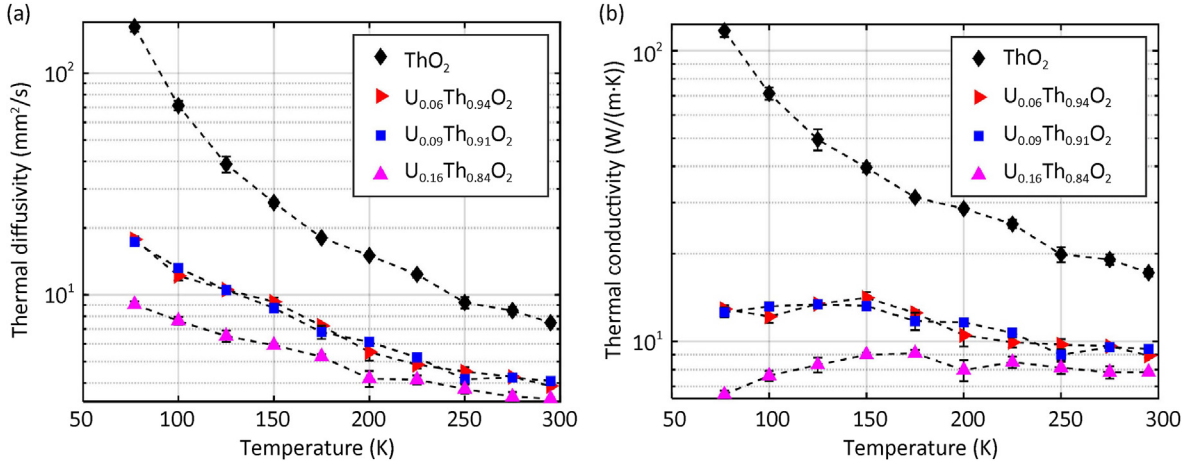

Fig. 2. Thermal diffusivity (left) and conductivity (right) measured using SDTR in the ThO_2 seed crystal, and iso-concentration regions of 6%, 9% and 16% uranium doping in ThO_2.

two terms (as shown with magenta line in Fig. 3 (right)). These optimized parameters, $A_i = 6.5 \times 10^{-44}$ s^3 and $B = 3.1 \times 10^{-18}$ s/K, are then held constant in further model fitting of U-doped thoria.

The scattering mechanisms attributed to U-doping are represented by the last two scattering terms. The third term in Eq. (3) describes phonon scattering by typical point defects using a general Rayleigh scattering expression with ω^4 dependence [9,48]. Here, Γ is the point defect scattering parameter, proportional to defect concentration [9,25]. The dashed green line in Fig. 3 (left) represents the best-fit KCM for 16% U-doped thoria with only the Rayleigh-type defect scattering term included in Eq. (3). This functional form is qualitatively unable to capture the trend apparent in the experimental results (*i.e.*, the hump in the k–T curve between 125 and 175 K), shown as red circles. The dashed blue line considers an alternate point defect scattering functional with an ω^2 dependence as an empirical attempt to fit the data. As can be seen, such an empirical attempt is able to better capture the experimental trend, though some qualitative deviation is still present, particularly at low temperatures.

The last term in Eq. (3) represents the phonon-spin interactions, which account for the time-dependent oscillating harmonic perturbation due to impurities or electronic degrees of freedom that resonate with phonons. The resonant frequency ω_0, stems from the transition energy gap between the spin states due to interaction with phonons, which simultaneously affects the phonon lifetime. The electron population differences between the levels involved in the spin transition is captured by $F(\omega_0, T) = \left(1 - e^{-\hbar\omega_0/k_B T}\right)/(1+e^{-\hbar\omega_0/k_B T})$ is a temperature-dependent distribution function [29,49,50]. The solid black line in Fig. 3 (left, and right) shows the fully optimized KCM taking into account both Rayleigh-type and phonon-spin interactions for the 16% U-doped region, which clearly captures the temperature dependence of the thermal conductivity. We then separate the influences on thermal conductivity from both effects. As shown in Fig. 3 (right), comparing with Rayleigh-type scattering (dashed green line), phonon-spin interactions (dot-dashed red line) impact thermal conductivity at a similar magnitude in the temperature region above 250 K and more significantly below. In this optimization, C_r (phonon-spin coupling constant) and Γ were used as local fitting parameters and ω_0 as a global fitting parameter for all three doping levels simultaneously, while B and A_i are determined from the seed region and held constant. The best-fit KCM parameters for all samples are summarized in Table 1, with the optimized k–T profiles for all three U-doped thoria regions presented in Fig. 4. The best-fit values for Γ and C_r scale monotonically with the U doping level, implying stronger phonon-spin interactions with a higher uranium concentration. However, we also find that C_r scales non-linearly with uranium concentration, varying little between the 6% and 9% doping levels.

Table 1
Optimized KCM fitting parameters for all U-doping levels measured. For doped regions, ω_0 is globally optimized for all conductivity data simultaneously.

	B(s/K)	A_i(s^3)	Γ	C_r(s^{-1})	ω_0(THz)
ThO_2	3.1×10^{-18}	6.51×10^{-44}			
$U_{0.06}Th_{0.94}O_2$	3.1×10^{-18}	6.51×10^{-44}	0.0204	1.15×10^{11}	3.83
$U_{0.09}Th_{0.91}O_2$	3.1×10^{-18}	6.51×10^{-44}	0.0206	1.29×10^{11}	3.83
$U_{0.16}Th_{0.84}O_2$	3.1×10^{-18}	6.51×10^{-44}	0.0214	5.89×10^{11}	3.83

While phonon-spin interactions related to the electronic structure of uranium have been previously studied [29,31], the measurements presented here provide the most direct investigation to date of the impact of this mechanism on phonon-mediated thermal transport in the U–ThO_2 system. Doping uranium into the host thoria lattice introduces 5f electrons not found in the ground state of thorium, the multipoles of which have been previously reported to interact strongly with phonons [51]. The presence of phonon-spin interactions in pure UO_2 has been confirmed by measuring the thermal conductivity of single crystal and polycrystalline UO_2 down to the liquid helium temperature [29,52]. Comparing to the k–T profile measured on thoria with the same fluorite structure, these studies concluded that phonon scattering from the 5f electronic degrees of freedom is responsible for the significantly lower thermal conductivity in UO_2.

We next compare the extracted parameters of the phonon transport model in this study to the ones presented by Gofryk and coworkers on pure UO_2 for insight into the scattering process [29]. In contrast to the model used here, Gofryk's work considered a two energy-level system to describe the spins of uranium ions, therefore with multiple resonances. The phonon resonant energy $h\omega_0$, converted from the resonant frequency, is comparable: ~2.5 meV here versus ~3.5 meV for one of the UO_2 resonances reported previously. The phonon-spin coupling constant C_r is also at the same order of magnitude: up to ~ 11×10^{11} s^{-1} for both resonances combined in UO_2, doubling the value measured on the 16% U-doped

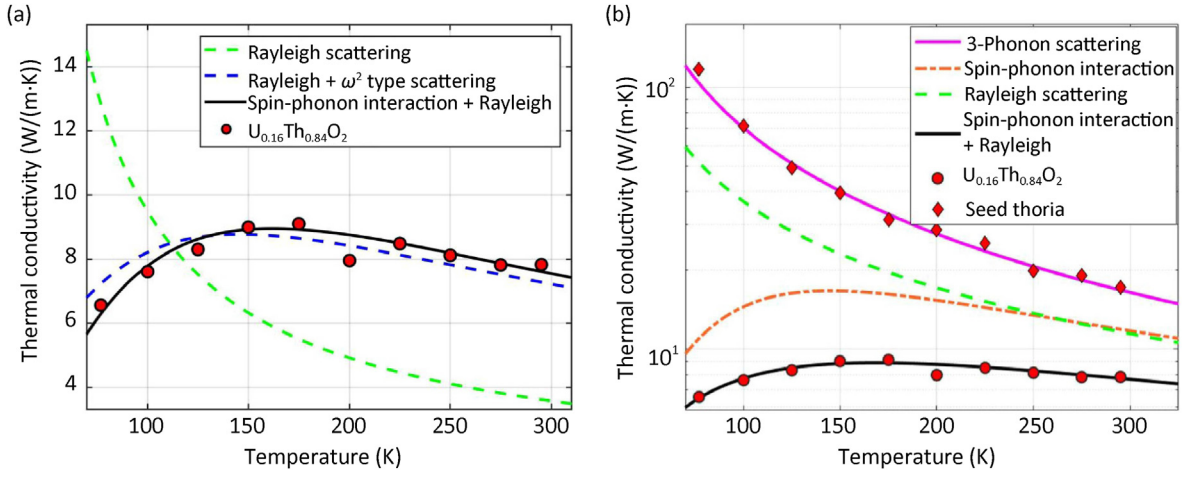

Fig. 3. Measured thermal conductivity of 16% U-doped thoria sample at low temperatures. (Left) Best fit curves using the KCM model with select scattering mechanisms: green dashed line – fit using only Rayleigh type point defect scattering; dashed blue line – fit including contribution from ω^2 type scattering mechanism along with Rayleigh scattering; solid black line – fit considering phonon-spin interactions in combination with Rayleigh scattering. (Right) Best-fit KCM model for 16% U-doped thoria showing the contributions of Rayleigh and phonon-spin interactions in comparison to the seed thoria crystal.

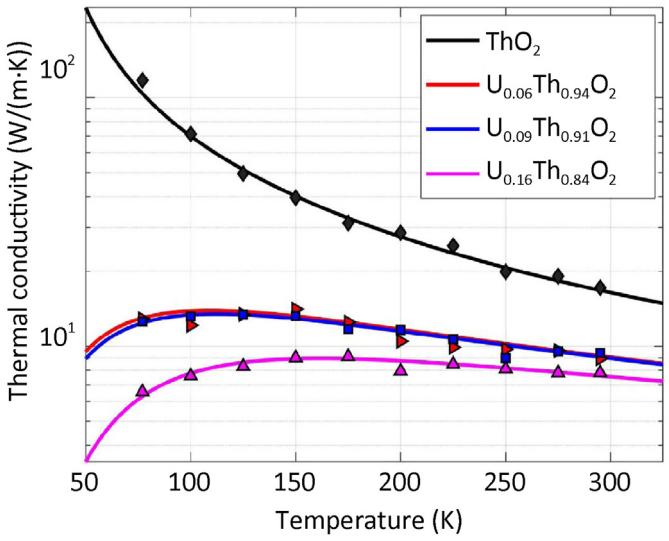

Fig. 4. KCM fit of the temperature dependent thermal conductivity profiles of pristine and all U-doped ThO_2. Markers show the experimentally measured thermal conductivity values and solid lines the best fit.

thoria (5.89×10^{11} s^{-1}). These comparisons, although from the simplified KCM approximation, support our hypothesis that the same phonon scattering mechanism exists in both UO_2 and U-doped ThO_2. The smaller-than-expected difference between U-doped thoria and pure UO_2 cases suggests that this phonon-spin interaction process has a nonlinear dependence on doping level, especially for higher levels of U doping than the ones used in this study. Otherwise, the ratio observed here would suggest a saturation in k reduction in the U–ThO_2 system with ~30%–35% U doping. We caution that only qualitative comparisons should be made between the bulk single crystal thermal conductivity measured in this work and the microcrystal measurements made by Gofryk and coworkers. In the latter case, boundary scatting effects known to significantly impact low temperature thermal conductivity must be explicitly accounted for [29] and radiative losses may also impact the as-measured values. In the case of the millimeter-scale single crystals measured here, using thermal waves localized to linear distances in the tens of microns, boundary scattering should play no significant role [26].

The nonlinear dependence of phonon-spin interactions on doping level can be extended to the low U doping region. With low U doping, differences between thermal transport in our 6% and 9% U-doped thoria are found negligible, but the difference between 6% U-doped thoria and pure thoria is significant, indicating an extreme sensitivity to the presence of any U-doping-induced phonon-spin interactions. To further explore the effects of very low concentrations of 5f electrons, future studies should expand to samples with lower U doping levels. In related studies of other material systems, phonon resonant scattering has been observed at much lower impurity concentrations than studied here (*e.g.*, 1×10^{19} cm^{-3} in Mn-doped GaN [21], and Ni– and Cr-doped ZnSe [53], equivalently ~0.1%–0.5%). These values provide a reasonable reference for targeted doping percentage ranges for future investigation.

4. Conclusion

In this work, the thermal conductivity of 6%, 9%, and 16% U-doped thoria was experimentally measured in the temperature range 77–300 K, and compared to calculations from a Klemens-Callaway phonon transport model to investigate the phonon scattering mechanisms in detail. Phonon-spin interactions induced by U doping are found to be more impactful on thermal conductivity suppression in the U–ThO_2 system than Rayleigh-type point defect scattering. Comparing the fitted parameters of our model to those reported in similar material systems with different doping percentages and in pure UO_2, we hypothesize that the relationship between the phonon-spin interaction intensity and the doping percentage is not linear, and it is likely that significant thermal conductivity reduction would appear with very low uranium doping percentages.

Data availability statement

The data that support the findings of this study are available from the corresponding author upon reasonable request.

Declaration of competing interest

The authors declare that they have no known competing financial interests or personal relationships that could have appeared to influence the work reported in this paper.

Acknowledgments

This work was supported by the Center for Thermal Energy Transport under Irradiation (TETI), an Energy Frontier Research Center funded by the US Department of Energy, Office of Science, Office of Basic Energy Sciences. The iso-concentration region analysis work was supported by the Air Force Research Laboratory under award FA807518D0015.

Appendix A. Supplementary data

Supplementary data to this article can be found online at https://doi.org/10.1016/j.jmat.2023.11.007.

References

[1] Mogensen M, Sammes NM, Tompsett GA. Physical, chemical and electrochemical properties of pure and doped ceria. Solid State Ionics 2000;129:63–94.
[2] Pan W, Phillpot SR, Wan C, Chernatynskiy A, Qu Z. Low thermal conductivity oxides. MRS Bull 2012;37:917–22.
[3] Zhao L-D, Tan G, Hao S, He J, Pei Y, Chi H, Wang H, Gong S, Xu H, Dravid VP, Uher C, Snyder GJ, Wolverton C, Kanatzidis MG. Ultrahigh power factor and thermoelectric performance in hole-doped single-crystal SnSe. Science 2016;351:141–4.
[4] Hurley DH, El-Azab A, Bryan MS, Cooper MWD, Dennett CA, Gofryk K, He H, Khafizov M, Lander GH, Manley ME, Mann JM, Marianetti CA, Rickert K, Selim FA, Tonks MR, Wharry JP. Thermal energy transport in oxide nuclear fuel. Chem Rev 2022;122:3711–62.
[5] Berman R. Heat conduction in solids. Oxford university press; 1976.
[6] Walker CT, Pohl RO. Phonon scattering by point defects. Phys Rev 1963;131:1433.
[7] Gibby R. The effect of plutonium content on the thermal conductivity of (U,Pu)O_2 solid solutions. J Nucl Mater 1971;38:163–77.
[8] Ohmichi T, Fukushima S, Maeda A, Watanabe H. On the relation between lattice parameter and O/M ratio for uranium dioxide-trivalent rare earth oxide solid solution. J Nucl Mater 1988;102:40–6.
[9] Klemens PG. The scattering of low-frequency lattice waves by static imperfections. Proc Phys Soc A 1955;68:1113.
[10] Abeles B. Lattice thermal conductivity of disordered semiconductor alloys at high temperatures. Phys Rev 1963;131:1906–11.
[11] Slack GA. Thermal conductivity of CaF_2, MnF_2, CoF_2, and ZnF_2 crystals. Phys Rev 1961;122:1451.
[12] Pohl RO. Thermal conductivity and phonon resonance scattering. Phys Rev Lett 1962;8:481.
[13] Slack GA, Galginaitis S. Thermal conductivity and phonon scattering by magnetic impurities in CdTe. Phys Rev 1964;133:A253.
[14] Kundu A, Otte F, Carrete J, Erhart P, Li W, Mingo N, Madsen GKH. Effect of local chemistry and structure on thermal transport in doped GaAs. Phys Rev Mater 2019;3:094602.
[15] Dongre B, Carrete J, Katre A, Mingo N, Madsen GK. Resonant phonon

scattering in semiconductors. J Mater Chem C 2018;6:4691–7.
[16] Dongre B, Carrete J, Wen S, Ma J, Li W, Mingo N, Madsen GK. Combined treatment of phonon scattering by electrons and point defects explains the thermal conductivity reduction in highly-doped Si. J Mater Chem A 2020;8:1273–8.
[17] Katre A, Carrete J, Dongre B, Madsen GK, Mingo N. Exceptionally strong phonon scattering by b substitution in cubic SiC. Phys Rev Lett 2017;119:075902.
[18] Maradudin AA. In: Theoretical and experimental aspects of the effects of point defects and disorder on the vibrations of crystals—2. Solid State Phys. Academic Press; 1967. p. 19.
[19] Mattuck R, Strandberg MWP. Spin-phonon interaction in paramagnetic crystals. Phys Rev 1960;119:1204.
[20] Toombs GA, Sheard FW. Use of the drone-fermion representation. ii. phonon scattering by paramagnetic ions. J Phys C Solid State Phys 1973;6:1467.
[21] Bagheri P, Reddy P, Kim JH, Rounds R, Sochacki T, Kirste R, Bockowski M, Collazo R, Sitar Z. Impact of impurity-based phonon resonant scattering on thermal conductivity of single crystalline GaN. Appl Phys Lett 2020;17:082101.
[22] Sun Q, Hou S, Wei B, Su Y, Ortiz V, Sun B, Lin JY, Smith H, Danilkin S, Abernathy DL, Wilson R, Li C. Spin-phonon interactions induced anomalous thermal conductivity in nickel (ii) oxide. Materials Today Physics 2023;35:101094.
[23] Herring JS, MacDonald PE, Weaver KD, Kullberg C. Low cost, proliferation resistant, uranium–thorium dioxide fuels for light water reactors. Nucl Eng Des 2001;203:65–85.
[24] Dennett CA, Hua Z, Khanolkar A, Yao T, Morgan PK, Prusnick TA, Poudel N, French A, Gofryk K, He L, Shao L, Khafizov M, Turner DB, Mann JM, Hurley DH. The influence of lattice defects, recombination, and clustering on thermal transport in single crystal thorium dioxide. Apl Mater 2020;8:111103.
[25] Deskins WR, Hamed A, Kumagai T, Dennett CA, Peng J, Khafizov M, Hurley DH, El-Azab A. Thermal conductivity of ThO_2: effect of point defect disorder. J Appl Phys 2021;129:075102.
[26] Dennett CA, Deskins WR, Khafizov M, Hua Z, Khanolkar A, Bawane K, Fu L, Mann JM, Marianetti C, He L, Hurley DH, El-Azab A. An integrated experimental and computational investigation of defect and microstructural effects on thermal transport in thorium dioxide. Acta Mater 2021;213:116934.
[27] Jin M, Dennett CA, Hurley DH, Khafizov M. Impact of small defects and dislocation loops on phonon scattering and thermal transport in ThO_2. J Nucl Mater 2022;566:153758.
[28] Deskins WR, Khanolkar A, Mazumder S, Dennett CA, Bawane K, Hua Z, Ferrigno J, He L, Mann JM, Khafizov M, Hurley DH, El-Azab A. A combined theoretical-experimental investigation of thermal transport in low-dose irradiated thorium dioxide. Acta Mater 2022;241:118379.
[29] Gofryk K, Du S, Stanek CR, Lashley JC, Liu XY, Schulze RK, Smith JL, Safarik DJ, Byler DD, McClellan KJ, Uberuagu BP, Scott BL, Andersson DA. Anisotropic thermal conductivity in uranium dioxide. Nat Commun 2014;5:1–7.
[30] Caciuffo R, Santini P, Carretta S, Amoretti G, Hiess A, Magnani N, Regnault LP, Lander GH. Multipolar, magnetic, and vibrational lattice dynamics in the low-temperature phase of uranium dioxide. Phys Rev B 2011;84:104409.
[31] Valu SO, Bona ED, Popa K, Griveau JC, Eric W, Konings RJM. The effect of lattice disorder on the low-temperature heat capacity of $(U_{1-y}Th_y)O_2$ and 238Pu-doped UO_2. Sci Rep 2019;9:1.
[32] Rickert K, Turner DB, Prusnick TA, Velez MA, Vangala S, Mann JM. The impact of feedstock size and composition on the hydrothermal growth of $(U,Th)O_2$. J Cryst Growth 2022;593:126732.
[33] Rickert K, Prusnick TA, Hunt E, Kimani MM, Chastang S, Brooks DL, et al. Inhibiting laser oxidation of UO_2 *via* Th substitution. J Nucl Mater 2019;517:254–62.
[34] Hua Z, Ban H, Khafizov M, Schley R, Kennedy R, Hurley DH. Spatially localized measurement of thermal conductivity using a hybrid photothermal technique. J Appl Phys 2012;111:103505.
[35] Hurley DH, Schley RS, Khafizov M, Wendt BL. Local measurement of thermal conductivity and diffusivity. Rev Sci Instrum 2015;86:123901.
[36] Maznev AA, Hartmann J, Reichling M. Thermal wave propagation in thin films on substrates. J Appl Phys 1995;78:5266–9.
[37] Hatori K, Taketoshi N, Baba T. Thermoreflectance technique to measure thermal effusivity distribution with high spatial resolution. Rev Sci Instrum 2005;76:114901.
[38] Mann JM, Thompson D, Serivalsatit K, Tritt TM, Ballato J, Kolis J. Hydrothermal growth and thermal property characterization of ThO_2 single crystals. Cryst Growth Des 2010;10:2146.
[39] Xiao E, Ma H, Bryan MS, Fu L, Mann JM, Winn B, et al. Validating first-principles phonon lifetimes *via* inelastic neutron scattering. Phys Rev B 2022;106:144310.
[40] Allen PB. Improved callaway model for lattice thermal conductivity. Phys Rev B 2013;88:144302.
[41] Ma J, Li W, Luo X. Examining the callaway model for lattice thermal conductivity. Phys Rev B 2014;90:035203.
[42] Callaway J. Model for lattice thermal conductivity at low temperatures. Phys Rev 1959;113:1046.
[43] Chauhan VS, Pakarinen J, Yao T, He L, Hurley DH, Khafizov M. Indirect characterization of point defects in proton irradiated ceria. Materialia 2021;15:101019.
[44] Mathis MA, Khanolkar A, Fu L, Bryan MS, Dennett CA, Rickert K, et al. Generalized quasiharmonic approximation *via* space group irreducible derivatives. Phys Rev B 2022;106:014314.
[45] Khanolkar A, Wang Y, Dennett CA, Hua Z, Mann JM, Khafizov M, Hurley DH. Temperature-dependent elastic constants of thorium dioxide probed using time-domain brillouin scattering. J Appl Phys 2023:133.
[46] Khafizov M, Park IW, Chernatynskiy A, He L, Lin J, Moore JJ, Swank D, Lillo T, Phillpot SR, El-Azab A, Hurley DH. Thermal conductivity in nanocrystalline ceria thin films. J Am Ceram Soc 2014;97:562–9.
[47] Ziman JM. Electrons and phonons: the theory of transport phenomena in solids. Oxford university press; 2001.
[48] Khafizov M, Pakarinen J, He L, Hurley DH. Impact of irradiation induced dislocation loops on thermal conductivity in ceramics. J Am Ceram Soc 2019;102:7533–42.
[49] Verma NGS. Phonon conductivity of trivalent rare-earth-doped gallium and aluminium garnets. Phys Rev B 1972;6:3509.
[50] Morton I, Lewis M. Effect of iron impurities on the thermal conductivity of magnesium oxide single crystals below room temperature. Phys Rev B 1971;3:552.
[51] Santini P, Carretta S, Amoretti G, Caciuffo R, Magnani N, Lander GH. Multipolar interactions in *f*-electron systems: the paradigm of actinide dioxides. Rev Mod Phys 2009;81:807.
[52] Moore JP, Mcelroy DL. Thermal conductivity of nearly stoichiometric single-crystal and polycrystalline UO_2. J Am Ceram Soc 1971;54:40.
[53] Lonchakov AT, Sokolov VI, Gruzdev NB. An unusually strong resonant phonon scattering by 3-*d* impurities in II–VI semiconductors. Phys Status Solidi 2004;1:2967.

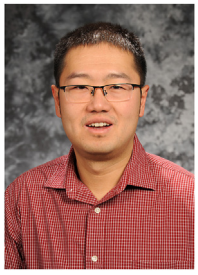

Dr. Zilong Hua is a staff scientist at Idaho National Laboratory with research interests in multi-scale thermal and acoustic transport phenomena of solid materials in extreme environment. Using laser-based characterization techniques, he has decades of experience of measuring and investigating thermal and mechanical property of pre- and post-irradiation materials. He also contributes to the development, deployment, and maintenance of state-of-art characterization techniques and INL-developed instruments, such as Thermal Conductivity Microscope (TCM) and Material Properties Microscope (MPM), for real-time, in situ measurements in reactors and hot cells. Dr. Hua received his doctorate in mechanical engineering at the Utah State University in 2013, and a bachelor's in materials science and engineering at the Tsinghua University (China) in 2007.